OPTICA

Detecting single nanoparticles using fiber-tip nanophotonics

Arthur L. Hendriks,[1,†,*] Daan Rabelink,[1,†] Mathias Dolci,[1] Paco Dreverman,[1] Mildred S. Cano-Velázquez,[1] Luca Picelli,[1] René P. J. van Veldhoven,[1] Peter Zijlstra,[1] Ewold Verhagen,[1,2] and Andrea Fiore[1]

[1]Department of Applied Physics and Science Education, and Eindhoven Hendrik Casimir Institute, Eindhoven University of Technology, 5600 MB, Eindhoven, The Netherlands
[2]Center for Nanophotonics, AMOLF, Science Park 104, 1098 XG, Amsterdam, The Netherlands
[†]These authors contributed equally to this work.
*a.l.hendriks@tue.nl

Received 2 January 2024; revised 17 February 2024; accepted 24 February 2024; published 16 April 2024

Sensing nano-objects, from nanoparticles to molecules, has become a crucial need in environmental monitoring, medical diagnostics, and drug development. Detection of single particles and molecules is highly desirable, as it provides specific information on size, dynamics, and interactions. Current nanophotonic implementations rely on complex optical readout schemes, limiting their application in the field. Here we demonstrate a nanophotonic fiber-tip sensor with a compact sensor footprint and a simple readout scheme. We leverage advanced design methods to simultaneously achieve a small mode volume $V_m = 0.74\,(\lambda/n)^3$, narrow linewidth $\Delta\lambda = 0.4$ nm, and a large modulation $\Delta R \approx 20\%$ in reflection from the fiber. This unique combination of properties opens the way to sensing weak nanoscale perturbations in the vicinity of the fiber tip. In particular, we experimentally demonstrate the real-time detection of single 50 nm nanoparticles. This opens a route towards real-time sensing of single nanoparticles, and potentially single molecules, in environmental monitoring and diagnostics.

https://doi.org/10.1364/OPTICA.516575

1. INTRODUCTION

The progress of nanoscience and nanotechnology has brought an increased understanding of the role of nano-objects in biological systems. For example, ultrafine particles (UFPs), i.e., particles with diameters below 100 nm, can pose serious health risks when inhaled, as they can penetrate deep into the most distal lung regions and have the capacity to absorb toxic organic compounds due to their relatively large surface area [1]. Due to their small size, they are difficult to measure without the use of bulky and expensive equipment in a laboratory setting [2]. For this reason, there is an increasing need for compact sensing solutions to be deployed in production environments and for environmental monitoring. Fiber-optic sensors are known to enable the accurate measurement of physical and chemical parameters at a distance, while being minimally invasive and insensitive to electromagnetic interference. However, due to the nature of fiber sensor manufacturing processes, the engineering of nanophotonic cavities for fiber sensing has remained limited. In particular, low-loss, wavelength-scale nanophotonic confinement, needed for sensing single nanoparticles and molecules, has not been achieved in the context of fiber sensing. The most common fiber sensors, fiber Bragg gratings (FBGs), rely on a weak periodic modulation of the refractive index over a centimeter-scale distance along the fiber. The corresponding narrow (sub-nanometer) reflection peak provides high wavelength imprecision and enables sensing temperature or strain in the fiber, but it is relatively insensitive to localized changes in the environment of the fiber. This makes FBGs unsuitable for measuring small particles or molecules and limits their application in biochemical and environmental sensing. In order to extend the functionalities of fiber sensors, a variety of "lab-on-fiber" technologies have been investigated, aimed at producing localized resonant structures within the fiber or on top of it [3,4]. Using these approaches, fiber-optic sensors for biological cells with dimensions in the micrometer range have been realized [5,6], and the detection of an average concentration of nanoparticles from a fiber tip has also been demonstrated [7,8]; however, sensing of single nanoparticles has not been achieved. Attempts at defining fiber-tip nanophotonic sensors are generally plagued by the difficulty of processing micro- and nano-structures on the fiber, as needed for optimal light confinement. As a possible solution, nanophotonic structures fabricated on a semiconductor wafer have been transferred to the fiber tip using various methods [9–12]. In particular, the transfer of photonic crystal cavities (PhCCs) stands out as a promising route, as PhCCs can feature extremely high quality factors (Q) together with ultrasmall mode volumes (V_m) [13,14]. These properties make them suitable for sensing localized refractive index changes, such as those induced by biomolecules or single particles [15–19].

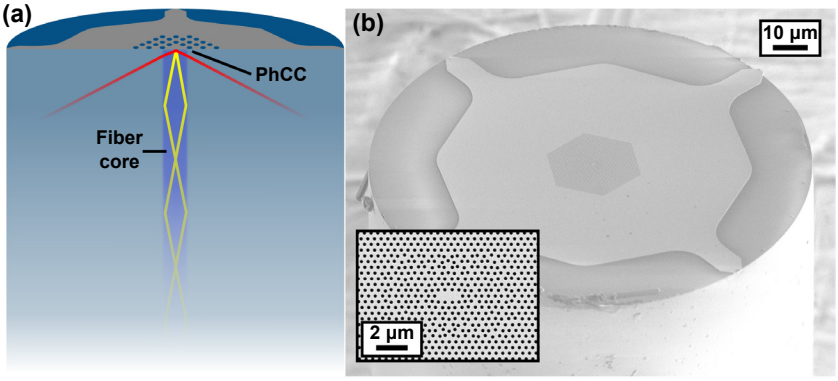

Fig. 1. (a) Sketch of a PhCC fiber-tip sensor, schematically showing the far-field emission of a standard PhCC (red) and the desired PhCC (yellow). (b) Transferred PhCC on the cleaved facet of a telecom fiber. Inset: close-up of the L3 cavity.

However, previous demonstrations of fiber-tip PhCCs have been limited by a relatively large mode size [20–23], limiting sensitivity, or poor coupling to the fiber mode [24,25], preventing an accurate measurement of the resonant wavelength in reflection. This is related to the large modal mismatch between the sub-micrometer PhCC resonance and the field of a single-mode fiber, which prevents their direct coupling. In fact, leakage from standard PhCCs predominantly occurs at large angles that do not couple to the fiber mode [Fig. 1(a)]. In this paper, we demonstrate the possibility to overcome this mismatch by advanced PhCC engineering, to achieve efficient, direct coupling between a highly localized PhCC mode and the fiber mode. Using this approach, and a simple and reproducible fiber-transfer method, we experimentally demonstrate fiber-tip sensors [Fig. 1(b)] with an unprecedented combination of high Q/V values and high visibility in reflection (reflection modulation $\Delta R \approx 20\%$). This allows us to achieve a wavelength imprecision down to 45 fm (more than three orders of magnitude lower than previous fiber-tip PhCCs demonstrations [7]), which, together with the small mode volume, provides an unprecedented sensitivity to local perturbations. Using these sensors, we demonstrate the real-time detection of single ultrafine particles in an aqueous environment, with diameters down to 50 nm, by directly probing the reflected power of the PhCC fiber tip.

2. RESULTS AND DISCUSSION

A. Simulations

Previous work aimed at improving the directivity of PhCCs focused on increasing the coupling into high numerical aperture (NA) collection lenses [26–29]. Most of these studies combine "gentle confinement" (fine tuning of the hole position to increase the Q-factor [30]) with band folding, where a subharmonic lattice is introduced by doubling the lattice constant [26,27]. In this work we make use of the L3 defect (three missing holes in a hexagonal lattice), which has shown small mode volumes and Q-factors that can be optimized by slight geometrical adjustments [14,30–32]. Figure 2(a) shows a standard L3 cavity with gentle confinement, while Fig. 2(b) displays the same cavity with gentle confinement and band folding. Gentle confinement acts by moving the holes at the side of the L3 cavity; this reduces the amount of light lost at large angles within the light cone, which increases the Q-factor [30]. The 10 holes closest to the cavity on the x axis are shifted, similarly to Ref [31]. The subharmonic lattice is defined by increasing the radius of every second hole around the L3 cavity in the x direction by an amount $dr = 0.06 \times a$, where a is the lattice constant. The far-field distributions in k-space of the PhCCs of Figs. 2(a) and 2(b) are shown in Figs. 2(d) and 2(e), respectively. These were simulated using the finite element method (FEM) software package COMSOL Multiphysics [33] (Supplement 1). We obtain an approximate estimation of the coupling efficiency η to the fundamental mode of the fiber by integrating the k-space electric field intensity (modulus square of the Fourier transform of the field) within the NA and dividing it by the corresponding integration over the light cone at the top and bottom of the slab (Supplement 1). For the standard L3 cavity the vertical outcoupling is low as there is little power radiated within the NA, whereas the intensity is maximal at the K-points on the x axis ($k_x = \frac{2}{3} \times \frac{2\pi}{a}$), resulting in a coupling efficiency into the fiber as low as 9×10^{-5}. When introducing the subharmonic lattice, the field at $k_x = \frac{\pi}{a}$ is folded over $k_x = \frac{\pi}{2a}$ resulting in a far-field component at $k_x = 0$ (Γ-point), which increases the coupling efficiency into the fiber for this perturbation to 8×10^{-3}. This band-folding principle has shown good results for coupling with external optics where a large numerical aperture (NA ≥ 0.5) is used [26,27]. However, the case of coupling to a standard single-mode fiber investigated here is much more challenging, due to the small NA $= 0.14$ [indicated with the white circle in Figs. 2(d)–2(f)]. In particular, the band folding also introduces additional loss in the light cone outside the fiber NA, substantially reducing the Q-factor [from 1850 for the cavity in Fig. 2(a) to 1085 for the cavity in Fig. 2(b)], even though only a small fraction of light is coupled to the desired output channel (i.e., the cavity is still heavily undercoupled). No substantial improvement was observed in a systematic set of simulations with different shifts and on different band-folded structures. We conclude that another approach is required to squeeze the far field more efficiently within the NA of the fiber while maintaining a high Q-factor.

To this aim, an open-source gradient-based optimization method based on semi-analytical guided mode expansion (GME) simulations was employed [34,35]. Its use for the optimization of the far-field of PhCCs in free-space applications was recently demonstrated in Ref [36]. This method is an efficient way to optimize PhC structures, but it remains an inherently approximate method. Therefore, we calculate the final coupling efficiency and Q-factor using COMSOL. Our L3-cavity is defined in a 250-nm-thick InP slab ($n_{\mathrm{InP}} = 3.165$) placed on top of a silica substrate

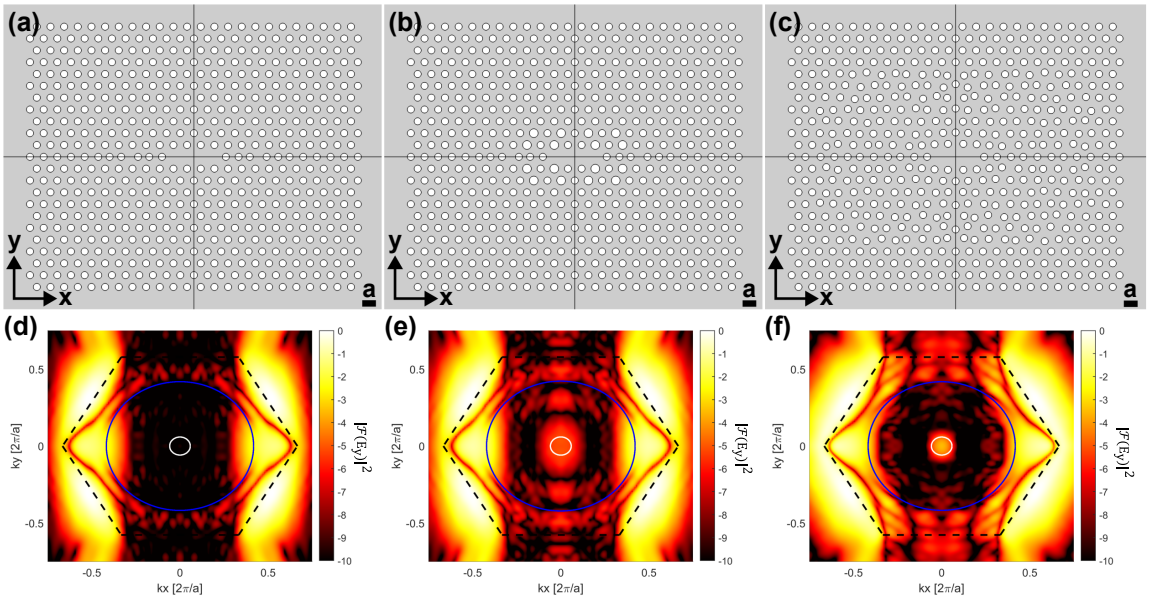

Fig. 2. (a) L3 cavity with gentle confinement; (b) L3 cavity with gentle confinement and band folding; (c) L3 cavity optimized for Q and coupling; (d)–(f) Normalized k-space distributions (modulus square of the Fourier transform of the y component of the E-field at the InP/silica interface, in logarithmic scale) for the cavity with gentle confinement (d); for the cavity with gentle confinement and band folding (e); and for the cavity optimized for Q and coupling (f). The white and blue circles represent the numerical aperture of the fiber and the light cone of the fiber, respectively. The dashed lines denote the first Brillouin zone.

($n_{\text{fiber}} = 1.468$) representing the fiber. The hexagonal PhC has a lattice constant of $a = 430$ nm and a hole radius of $r = 0.26 \times a$. The L3 cavity is defined by removing three holes at the center of a supercell made of 20 columns and 14 rows, with periodic boundary conditions. In the top right quadrant there are 82 holes. These holes are shifted with respect to their original positions by factors $dx \times a$ and $dy \times a$ in the x and y directions, respectively, which is mirrored to the other quadrants, to maximize the objective function

$$f = \tan^{-1}\left(\frac{Q}{Q_0}\right) \times \frac{\sum_{k_{\text{NA}}} |d_i|^2}{\sum_{k_{\text{LC}}} |d_i|^2 - \sum_{k_{\text{NA}}} |d_i|^2} \times |\mathbf{E}(\mathbf{r}=0)|^2, \tag{1}$$

where the quality factor, the efficiency, and the mode volume are optimized. The first factor of Eq. (1) increases the quality factor (Q) towards a target quality factor (Q_0), where the inverse tangent is used as a weighting factor [36]. The second factor of Eq. (1) increases the ratio of the loss rates into the NA of the fiber to all the other radiative losses. Here the loss rates are estimated from the sum of the squared moduli of the coupling constants d_i, which describe the coupling between the cavity and output fields [37], within the NA of the fiber ($\sum_{k_{\text{NA}}} |d_i|^2$) and within the light cone at both sides of the slab ($\sum_{k_{\text{LC}}} |d_i|^2$). The last factor of Eq. (1) increases the electric field $\mathbf{E}$ at the center of the cavity to minimize the mode volume. Typically after 20–30 optimization iterations the function reaches a maximum for the coupling efficiency. Our script is publicly available for use by the community [38]. The responses for the final obtained values of dx and dy (Supplement 1) (for all holes) are then simulated using COMSOL. A result of the optimization can be seen in Fig. 2(c), where a target $Q_0 = 10^4$ was used (the in-plane field distribution for this mode is provided in the Supplement 1). In the respective k-space distribution [Fig. 2(f)] it can be seen that the far field is more tightly confined within the NA while simultaneously having much lower components between the NA and the light cone as compared to the band-folded case. The coupling efficiency from the finite element analysis is found to be around $\eta = 0.126$ together with a Q-factor of 4400. Compared to the band-folded case the coupling efficiency is 16 times higher and the Q-factor is 4 times higher. This comes with the added benefit, compared to the band-folding approach, that the hole radius is constant, which makes the design more robust to fabrication imperfections.

B. Optimization Limits

We further explored the limits of the optimization. First, the fact that the cavity is placed on a fiber decreases the achievable Q-factor considerably, due to the larger light cone. This is seen in the optimization results for different target Q_0 of Eq. (1) [Fig. 3(a)], where the Q is limited to a maximum value of 5030, for a PhCC on glass, while it reaches much higher values for a cavity suspended in air. This is in line with previous reports of PhCCs on dielectric substrates [24,39,40]. The second limit is that the NA of a single mode (SM) fiber is very small, which limits the achievable coupling efficiency. This is seen in the k-space plot of Fig. 2(f), where the central spot extends beyond the white circle representing the fiber NA. To confirm this observation, in Fig. 3(b) the coupling efficiency is optimized for different NAs for the suspended cavity ("air–air") and the cavity on glass ("air–fiber"). The efficiency of the cavity on fiber is always lower, which we attribute to the larger light cone. As expected, the efficiency increases for higher NA, where at an NA = 0.4 a value of $\eta = 0.43$ for the suspended case is reached (as compared to the ideal value of $\eta = 0.5$ for single-sided collection), due to leakage at the edges of the light cone. The trade-off between efficiency and Q is analyzed in Fig. 3(c), where the points represent the Q and η values obtained from the optimizations with different Q_0 targets, for two different NAs (0.14 and 0.3) for suspended and on-fiber cavities. The band-folded design of

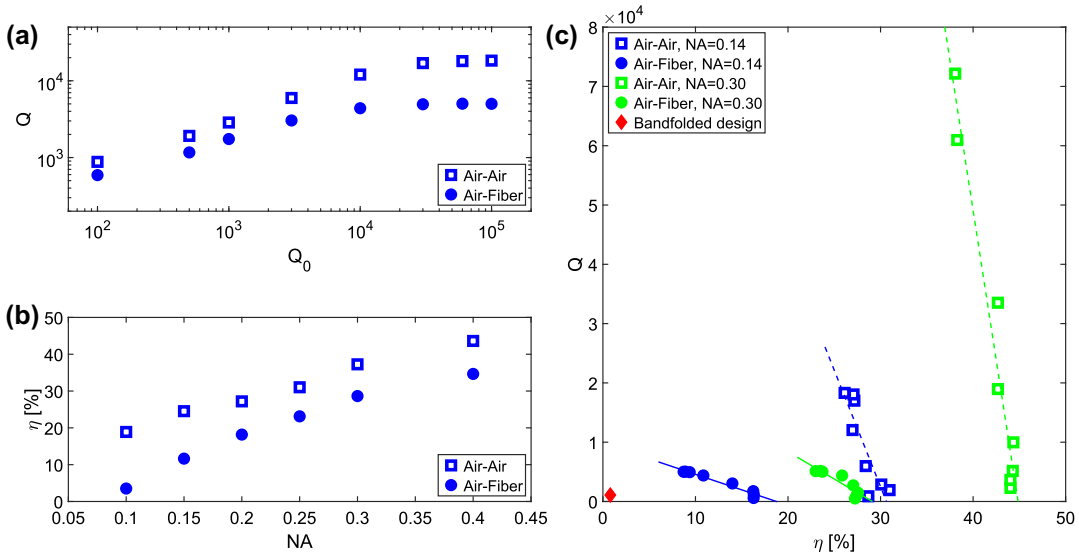

Fig. 3. (a) Simulated Q-factors of optimized cavities as a function of optimization parameter Q_0, for suspended PhCCs cladded by air on both sides ("air–air"), and for PhCCs on fiber ("air–fiber"), for an NA = 0.14. (b) Simulated coupling efficiencies of cavities optimized for different numerical apertures, for a target $Q_0 = 10^4$. (c) Q-factor as a function of efficiency, for different Q_0, for "air–air" and "air–fiber" cavities for two NAs (0.14 and 0.3). The continuous and dashed lines are linear fits.

Fig. 2(b) is also reported for comparison. As expected, the increase in Q with increasing Q_0, observed in Fig. 3(a), comes at a cost of reduced efficiency. By increasing the NA, this trade-off is shifted, enabling higher efficiencies at the same Q-factor. On the other hand, suspending the cavity increases both Q and η. While there is no guarantee that the optimization method provides global maxima of the objective function, the observed trade-offs suggest that we are probing the physical limits of loss and coupling. We note that, while in this work we focus on PhCCs in physical contact with the fiber and on a standard SM fiber, these are not fundamental limitations, as it is possible to transfer suspended membranes on fiber tips [41], and SM fibers with NAs up to 0.41 are commercially available [42].

C. Characterization

The PhCCs were fabricated on a 250-nm-thick InP membrane using standard semiconductor nanofabrication and then transferred to the fiber tips using the approach demonstrated in Ref. [9] (Supplement 1). An electron-microscope image of the optimized L3 cavity on fiber is shown in Fig. 1(b). After the transfer, the PhCC is measured in reflectance through the fiber, using a superluminescent diode (SLED), a 50:50 fiber-optic coupler, a manual fiber polarization controller, and an optical spectrum analyzer (OSA). The absolute reflectance is derived by dividing the spectrum from the fiber-tip PhCC by a reference spectrum obtained by replacing the sensor with a fiber-optic retroreflector. We swept the Q_0 parameter of the objective function [Eq. (1)] from 10^2 to 10^5, fabricated the PhCCs, and measured them experimentally. The Q_0 parameter sweep was used in order to experimentally confirm the possibility of controlling the Q-factor. Three reflectance spectra of fiber-tip sensors with different Q_0 can be seen in Fig. 4(a). Using coupled mode theory, a fitting function is derived (Supplement 1). The corresponding experimental values for the efficiencies and Q-factors from the fitting function are compared to the simulated ones in Fig. 4(b). Both the efficiency and Q-factor show the expected trends with the target Q_0 and are in agreement with the simulated values, except for a lower value of the experimental Q-factor, which is most likely due to fabrication imperfections. It should be noted that the efficiency is highly dependent on the alignment of the fiber with the center of the cavity, where minor deviations decrease the efficiency severely. This is reflected in the error bars in Fig. 4(b), which denote the standard deviation of repetitive transfers on similar structures (with high Q_0). Overall Fig. 4(b) shows we can reproducibly achieve Q-factors of few 1000s together with coupling efficiencies >10%. The obtained combination of Q/V values and modulations depths are considerably larger than other demonstrated fiber-tip sensors [22,43–45]. In particular, the only other demonstrations of wavelength-scale optical confinement on fiber tips did not probe the resonance directly in reflection, but made use of photoluminescence of embedded quantum dots [7,24,25], severely limiting the practical application.

D. Ultrafine Particle Sensing

The optimized L3 cavity on the fiber tip can be used as a precise sensor of refractive index (RI), with a low limit of detection (LOD) (Supplement 1). While bulk RI sensing does not require a small mode volume, the unique features of our nanophotonic fiber sensor are essential when detecting individual nano-scale objects, such as single nanoparticles. Here we take advantage of the unique combination of ultrasmall mode volume and wavelength imprecision, to demonstrate fiber sensing of single nanoparticles. Two aqueous suspensions of positively charged amine-coated polystyrene particles ($n = 1.56$) with a diameter of 200 nm (weight fraction $= 2 \times 10^{-5}$ and concentration $= 4.5 \times 10^9$ particles/ml) and 50 nm (weight fraction $= 5 \times 10^{-6}$ and concentration $= 7.2 \times 10^8$ particles/ml) are used. The sensor surface is activated using plasma cleaning, giving rise to negatively charged hydroxyl groups. This leads to electrostatic interactions causing nanoparticle adsorption onto the fiber-tip surface in a random fashion. Other configurations are also possible where particles are electrostatically charged before detection [46], negatively

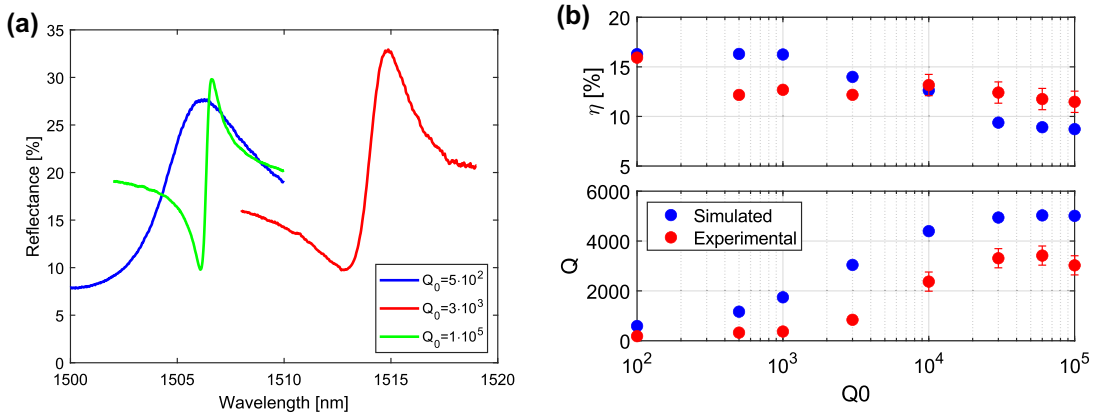

Fig. 4. (a) Reflectance spectrum of fiber-tip PhCCs optimized for different target Q_0. (b) Comparison between simulated and experimental values of η and Q for a sweep in Q_0.

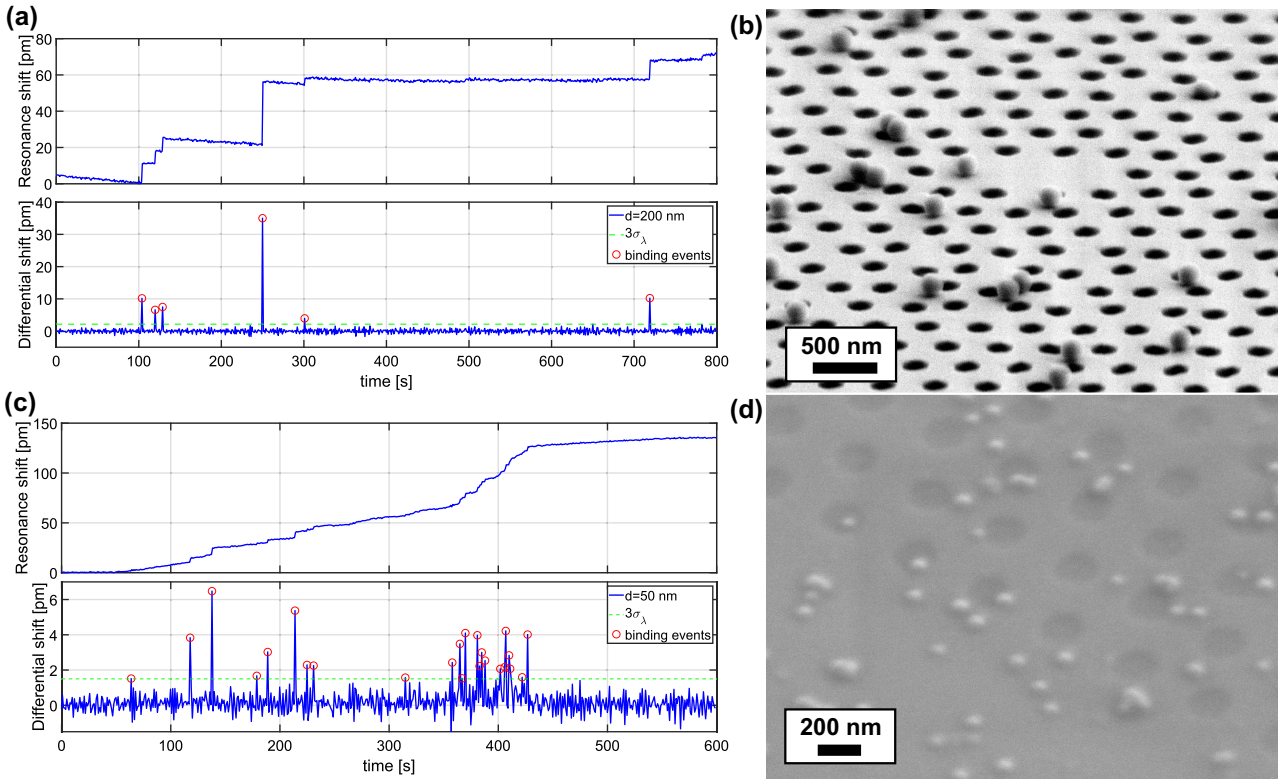

Fig. 5. (a) Resonance and differential shift over time for digital binding events of 200 nm diameter particles. (b) SEM image of 200 nm particles near the center of the L3 cavity. (c) Resonance and differential shift over time for digital binding events of 50 nm diameter particles. (d) SEM image of 50 nm particles on the surface of the fiber-tip sensor.

charged particles are detected by a positively charged surface with polyelectrolyte [47], or particles are accelerated towards the sensor surface, which is coated with an adhesive [48]. A constant flow of deionized water at 50 µL/min was used in the first 30 min to stabilize the temperature of the sensor. Afterwards, the particles were flown past the fiber-tip sensors at 50 µL/min (Supplement 1). In Fig. 5(a) the progressing shift in fitted resonant wavelength and the differential shift can be seen with an integration time of 1 s for the 200 nm particles using an optical interrogator. Multiple discrete red shifts are observed and are attributed to single-particle binding events, based on the criterion that the differential shift is larger than the LoD $= 3\sigma_\lambda$ ($\sigma_\lambda = 0.5$ pm in these experiments). The discreteness of the shifts makes it straightforward to differentiate them from gradual changes in the bulk refractive index or temperature. This attribution was further confirmed by taking electron-microscope images at the end of the experiment. The particles that induced the resonance shift can be seen close to the L3 cavity [Fig. 5(b)]. The range in shifts is caused by the exact binding position within the PhCC mode volume, as we assume that the size and refractive index are monodispersed. UFPs with a diameter of 50 nm were also detected as seen in Fig. 5(c), where more than 20 binding events were identified. This experiment was repeated several times on different fiber-tip sensors and compared to simulations, which show a good agreement of wavelength shift (Supplement 1). We note that, differently from previous demonstrations of single-particle sensing using on-chip PhCCs

[18], microcavities [49,50], and plasmonic sensors [51–53], our approach requires no coupling optics and uses commercial fiber-optic interrogation equipment, making it readily applicable to practical application cases. According to perturbation theory and simulations, the wavelength imprecision of $\sigma_\lambda = 45$ fm obtained with fixed-wavelength interrogation (Supplement 1) provides a detection limit of 12 nm particles (Supplement 1). This assumes that the nanoparticles land exactly at the center of the cavity, and indicates that large biomolecular complexes such as IgM, viruses, and extracellular vesicles may be detectable. This number could be further improved by using PhCCs with smaller mode volumes, such as H1 or H0 cavities [31], higher Q, and improved interrogation. With these improvements it could be possible to approach the fundamental thermodynamic limit [54,55] and sense single biomolecules [18,49,51–53], such as antibodies or inflammatory proteins.

3. CONCLUSIONS

We demonstrate a nanophotonic fiber-tip sensor that combines the unique advantages of semiconductor nanophotonic cavities with the readout convenience of fiber sensors. To this aim, we simultaneously optimize the quality factor, mode volume, and fiber coupling efficiency of a photonic crystal cavity using a gradient-based optimization method. These cavities were realized using standard nanofabrication methods and transferred to the fiber facet using a scalable wafer-to-fiber transfer technique. As a result, we obtain a fiber-tip sensor with an unprecedented combination of quality factor, mode confinement, and reflectance modulation. These PhCC fiber-tip sensors can be used for refractive index sensing with a low limit of detection and for real-time detection of single ultrafine particles with diameters down to few 10 s of nanometers, which may have relevant applications in environmental monitoring. By further optimizing the cavity design, the interrogation system, and biofunctionalization of the PhCC surface [56], this approach could also enable the detection of single biomolecules with high specificity. Besides the immediate applications to industrial sensing, biosensing, and air-quality monitoring, the proposed combination of semiconductor nanophotonics and fiber sensing represents a new avenue for the practical application of advanced nanophotonic devices. By using higher NA fibers and suspended structures, nanophotonic cavities with best-in-class characteristics can be directly coupled and interrogated through single-mode fibers, with no coupling optics, dramatically reducing packaging complexity and cost for nanophotonic devices ranging from single-photon emitters to nano-optomechanical sensors.

Funding. Nederlandse Organisatie voor Wetenschappelijk Onderzoek (NOW) (TTW project No. 18477); Zwaartekracht Research Center for Integrated Nanophotonics (024.002.033). This research was funded by NWO (A.L.H., M.D., and M.S.C.V.) and by NWO Zwaartekracht Research Center for Integrated Nanophotonics (L.P. and R.P.J.v.V.).

Acknowledgment. We are grateful to Dr. Momchil Minkov for the valuable discussions on the optimization program. We are thankful to Matteo Lodde for taking the electron microscope image shown in Fig. 5(b).

Disclosures. The authors declare no competing interests.

Data availability. The data that support the findings of this work are available from the corresponding author upon reasonable request.

Supplemental document. See Supplement 1 for supporting content.

REFERENCES

1. H. S. Kwon, M. H. Ryu, and C. Carlsten, "Ultrafine particles: unique physicochemical properties relevant to health and disease," Exp. Mol. Med. **52**, 318–328 (2020).
2. J. Marval and P. Tronville, "Ultrafine particles: A review about their health effects, presence, generation, and measurement in indoor environments," Build. Environ. **216**, 108992 (2022).
3. A. Cusano, M. Consales, A. Crescitelli, *et al.*, *Lab-on-Fiber Technology* (Springer, 2015).
4. M. Pisco and A. Cusano, "Lab-on-fiber technology: a roadmap toward multifunctional plug and play platforms," Sensors **20**, 4705 (2020).
5. R. S. Rodrigues Ribeiro, P. Dahal, A. Guerreiro, *et al.*, "Fabrication of Fresnel plates on optical fibres by FIB milling for optical trapping, manipulation and detection of single cells," Sci. Rep. **7**, 1–14 (2017).
6. J. S. Paiva, P. A. Jorge, R. S. Ribeiro, *et al.*, "iLoF: an intelligent lab on fiber approach for human cancer single-cell type identification," Sci. Rep. **10**, 1–16 (2020).
7. G. Shambat, S. Rajasekhar Kothapalli, A. Khurana, *et al.*, "A photonic crystal cavity-optical fiber tip nanoparticle sensor for biomedical applications," Appl. Phys. Lett. **100**, 213702 (2012).
8. J. S. Paiva, P. A. Jorge, R. S. Ribeiro, *et al.*, "Optical fiber-based sensing method for nanoparticle detection through supervised back-scattering analysis: a potential contributor for biomedicine," Int. J. Nanomed. **14**, 2349–2369 (2019).
9. L. Picelli, A. Van Klinken, G. Lindgren, *et al.*, "Scalable wafer-to-fiber transfer method for lab-on-fiber sensing," Appl. Phys. Lett. **117**, 151101 (2020).
10. E. J. Smythe, M. D. Dickey, B. Jiming, *et al.*, "Optical antenna arrays on a fiber facet for in situ surface-enhanced Raman scattering detection," Nano Lett. **9**, 1132–1138 (2009).
11. D. J. Lipomi, R. V. Martinez, M. A. Kats, *et al.*, "Patterning the tips of optical fibers with metallic nanostructures using nanoskiving," Nano Lett. **11**, 632–636 (2011).
12. M. Boerkamp, Y. Lu, J. Mink, *et al.*, "Multiple modes of a photonic crystal cavity on a fiber tip for multiple parameter sensing," J. Lightwave Technol. **33**, 3901–3906 (2015).
13. M. Notomi, "Manipulating light with strongly modulated photonic crystals," Rep. Prog. Phys. **73**, 096501 (2010).
14. T. Asano, Y. Ochi, Y. Takahashi, *et al.*, "Photonic crystal nanocavity with a Q factor exceeding eleven million," Opt. Express **25**, 1769–1777 (2017).
15. P. M. Fauchet and M. R. Lee, "Nanoscale microcavity sensor for single particle detection," Opt. Lett. **32**, 3284–3286 (2007).
16. A. Di Falco, L. O'Faolain, and T. F. Krauss, "Chemical sensing in slotted photonic crystal heterostructure cavities," Appl. Phys. Lett. **94**, 63503 (2009).
17. R. T. Chen, Y. Zou, S. Chakravarty, *et al.*, "Silicon nano-membrane based photonic crystal microcavities for high sensitivity bio-sensing," Opt. Lett. **37**, 1208–1210 (2012).
18. Q. Quan, D. L. Floyd, I. B. Burgess, *et al.*, "Single particle detection in CMOS compatible photonic crystal nanobeam cavities," Opt. Express **21**, 32225–32233 (2013).
19. Y. N. Zhang, Y. Zhao, and R. Q. Lv, "A review for optical sensors based on photonic crystal cavities," Sens. Actuators A Phys. **233**, 374–389 (2015).
20. B. Park, J. Provine, I. W. Jung, *et al.*, "Photonic crystal fiber tip sensor for high-temperature measurement," IEEE Sens. J. **11**, 2643–2648 (2011).
21. D. Yang, H. Tian, and Y. Ji, "Optical fiber tips integrated with high-Q Fano-resonance pillar-array photonic-crystals for high sensitive remote sensing," in *Asia Communications and Photonics Conference* (2015), paper AS4I.5.
22. S. Zhang, S. J. Tang, S. Feng, *et al.*, "High-Q polymer microcavities integrated on a multicore fiber facet for vapor sensing," Adv. Opt. Mater. **7**, 1900602 (2019).
23. L. Picelli, P. J. van Veldhoven, E. Verhagen, *et al.*, "Hybrid electronic-photonic sensors on a fibre tip," Nat. Nanotechnol. **18**, 1162–1167 (2023).
24. G. Shambat, J. Provine, K. Rivoire, *et al.*, "Optical fiber tips functionalized with semiconductor photonic crystal cavities," Appl. Phys. Lett. **99**, 191102 (2011).
25. B. Wang, T. Siahaan, M. A. Dündar, *et al.*, "Photonic crystal cavity on optical fiber facet for refractive index sensing," Opt. Lett. **37**, 833–835 (2012).

26. N. V. Q. Tran, S. Combrié, P. Colman, *et al.*, "Vertical high emission in photonic crystal nanocavities by band-folding design," Phys. Rev. B **82**, 075120 (2010).
27. S. L. Portalupi, M. Galli, C. Reardon, *et al.*, "Planar photonic crystal cavities with far-field optimization for high coupling efficiency and quality factor," Opt. Express **18**, 16064–16073 (2010).
28. H. Takagi, Y. Ota, N. Kumagai, *et al.*, "High Q H1 photonic crystal nanocavities with efficient vertical emission," Opt. Express **20**, 28292–28300 (2012).
29. S. Iwamoto, Y. Ota, and Y. Arakawa, "Asymmetric out-of-plane power distribution in a two-dimensional photonic crystal nanocavity," Opt. Lett. **40**, 3372–3375 (2015).
30. Y. Akahane, T. Asano, B. S. Song, *et al.*, "High-Q photonic nanocavity in a two-dimensional photonic crystal," Nature **425**, 944–947 (2003).
31. M. Minkov and V. Savona, "Automated optimization of photonic crystal slab cavities," Sci. Rep. **4**, 1–8 (2014).
32. J. P. Vasco and V. Savona, "Global optimization of an encapsulated Si/SiO2 L3 cavity with a 43 million quality factor," Sci. Rep. **11**, 1–6 (2021).
33. "COMSOL Multiphysics v. 6.1," COMSOL AB, https://www.comsol.com.
34. M. Minkov, I. A. Williamson, L. C. Andreani, *et al.*, "Inverse design of photonic crystals through automatic differentiation," ACS Photonics **7**, 1729–1741 (2020).
35. "Legume: Guided Mode Expansion supporting automatic differentiation with autograd," Available via the Internet at: https://github.com/fancompute/legume (accessed January 2, 2024).
36. C. L. Panuski, I. Christen, M. Minkov, *et al.*, "A full degree-of-freedom spatiotemporal light modulator," Nat. Photonics **16**, 834–842 (2022).
37. Y. Guo, M. Xiao, and S. Fan, "Topologically protected complete polarization conversion," Phys. Rev. Lett. **119**, 167401 (2017).
38. "PhCC on fiber-tip based on legume". Available via the Internet at: https://github.com/alhendriks/PhCC_on_Fiber-tip (accessed February 16, 2024).
39. Y. Tanaka, T. Asano, R. Hatsuta, *et al.*, "Investigation of point-defect cavity formed in two-dimensional photonic crystal slab with one-sided dielectric cladding," Appl. Phys. Lett. **88**, 12 (2006).
40. E. Kuramochi, H. Taniyama, T. Tanabe, *et al.*, "Ultrahigh-*Q* one-dimensional photonic crystal nanocavities with modulated mode-gap barriers on SiO2 claddings and on air claddings," Opt. Express **18**, 15859–15869 (2010).
41. A. L. Hendriks, L. Picelli, P. V. Veldhoven, *et al.*, "Nano-optomechanics on a fiber-tip," in *12th International Conference on Metamaterials, Photonic Crystals and Plasmonics, META* (META, 2022).
42. Thorlabs, "UHNA7 ultra-high NA silica fiber, 0.41 NA, 1500-2000 nm."
43. M. Consales, A. Ricciardi, A. Crescitelli, *et al.*, "Lab-on-fiber technology: toward multifunctional optical nanoprobes," ACS Nano **6**, 3163–3170 (2012).
44. L. X. Kong, Y. X. Zhang, W. G. Zhang, *et al.*, "Lab-on-tip: protruding-shaped all-fiber plasmonic microtip probe toward in-situ chem-bio detection," Sens. Actuators B Chem. **301**, 127128 (2019).
45. M. S. Cano-Velázquez, A. L. Hendriks, L. Picelli, *et al.*, "Temperature-compensated solution concentration measurements using photonic crystal fiber-tip sensors," Sensors **23**, 7703 (2023).
46. C. Zhang, R. Zhu, and W. Yang, "A micro aerosol sensor for the measurement of airborne ultrafine particles," Sensors **16**, 399 (2016).
47. H. Hartmann and R. Krastev, "Biofunctionalization of surfaces using polyelectrolyte multilayers," BioNanoMaterials **18**, 20160015 (2017).
48. X. Qin, X. Xian, Y. Deng, *et al.*, "Micro quartz tuning fork-based PM 2.5 sensor for personal exposure monitoring," IEEE Sens. J. **19**, 2482–2489 (2019).
49. F. Vollmer, S. Arnold, and D. Keng, "Single virus detection from the reactive shift of a whispering-gallery mode," Proc. Natl. Acad. Sci. USA **105**, 20701–20704 (2008).
50. T. Lu, H. Lee, T. Chen, *et al.*, "High sensitivity nanoparticle detection using optical microcavities," Proc. Natl. Acad. Sci. USA **108**, 5976–5979 (2011).
51. I. Ament, J. Prasad, A. Henkel, *et al.*, "Single unlabeled protein detection on individual plasmonic nanoparticles," Nano Lett. **12**, 1092–1095 (2012).
52. P. Zijlstra, P. M. Paulo, and M. Orrit, "Optical detection of single non-absorbing molecules using the surface plasmon resonance of a gold nanorod," Nat. Nanotechnol. **7**, 379–382 (2012).
53. A. B. Taylor and P. Zijlstra, "Single-molecule plasmon sensing: current status and future prospects," ACS Sens. **2**, 1103–1122 (2017).
54. K. Saurav and N. L. Thomas, "Probing the fundamental detection limit of photonic crystal cavities," Optica **4**, 757–763 (2017).
55. C. Panuski, D. Englund, and R. Hamerly, "Fundamental thermal noise limits for optical microcavities," Phys. Rev. X **10**, 041046 (2020).
56. S. Dey, M. Dolci, and P. Zijlstra, "Single-molecule optical biosensing: recent advances and future challenges," ACS Phys. Chem. Au **3**, 143–156 (2023).